

Ultra-compact optical true time delay device for wideband phased array radars

Betty Lise Anderson^{*a}, James G. Ho^b, William D. Cowan^c, Olga B. Spahn^c, Allen Y. Yi^d, Martin R. Flannery^b, Delton J. Rowe^b, David L. McCray^d, David J. Rabb^e, Peter Chen^b

^aThe Ohio State University Department of Electrical and Computer Engineering, 205 Dreese Laboratory, 2015 Neil Avenue, Columbus OH USA 43210; ^bNorthrop Grumman Aerospace Systems, 1 Space Park, Redondo Beach, CA 90278; ^cSandia National Laboratories, PO Box 5800, Mail Stop 0603, Albuquerque, NM 87185, ^dThe Ohio State University Department of Integrated Systems Engineering, 242 Baker Systems Hall, 1971 Neil Avenue, Columbus OH 43210; ^enow with AFRL/RYSJM, 3109 Hobson Way, WPAFB OH 45433-7700

ABSTRACT

An ultra-compact optical true time delay device is demonstrated that can support 112 antenna elements with better than six bits of delay in a volume 16”x5”x4” including the box and electronics. Free-space beams circulate in a White cell, overlapping in space to minimize volume. The 18 mirrors are slow-tool diamond turned on two substrates, one at each end, to streamline alignment. Pointing accuracy of better than 10 μ rad is achieved, with surface roughness \sim 45 nm rms. A MEMS tip-style mirror array selects among the paths for each beam independently, requiring \sim 100 μ s to switch the whole array. The micromirrors have 1.4 $^\circ$ tip angle and three stable states (east, west, and flat). The input is a fiber-and-microlens array, whose output spots are re-imaged multiple times in the White cell, striking a different area of the single MEMS chip in each of 10 bounces. The output is converted to RF by an integrated InP wideband optical combiner detector array. Delays were accurate to within 4% (shortest delay) to 0.03% (longest mirror train). The fiber-to- detector insertion loss is 7.82 dB for the shortest delay path.

Keywords: true time delay, phased array radar, MEMS, slow-tool diamond turning,

1. INTRODUCTION

Wide-band phased arrays generally use true time delay (TTD) to steer the radar beam rather than phase-shifting, in order to avoid beam squint. In an optical TTD, there is one light beam for each antenna in the array, and each light beam passes through a path of variable length to incur the delays. Typical approaches use variable lengths of fiber [1-4], or wavelength tuning to take advantage of fiber dispersion [5, 6] or chirped Bragg gratings [7-9]. We report here on an optical TTD based on the White cell [10], a free-space system in which an array of input beams circulates among a system of mirrors and is re-imaged to a set of spots on a microelectromechanical systems (MEMS) mirror array. The micromirrors tilt to select among paths of various lengths for each light beam individually.

The basic principle of the White cell is described in detail elsewhere [10, 11]. Briefly, the original White cell consists of a pair of identical spherical mirrors facing a third, Figure 1a. Each of $Z1$ and $Z2$ images onto the other through the field mirror M , and the field mirror images back onto itself through either of the two objective mirrors $Z1$ or $Z2$. The objective mirrors are aligned such that they produce a set of successive images of the input spot array on the field mirror, Figure 1(b). Input and output turning mirrors are adjacent to the field mirror for I/O. For TTD, we replace the field mirror with a MEMS tilt-style micromirror array and a field lens. On each bounce, each light beam can be independently switched to different White cell objective mirrors at varying distances, to produce the time delay.

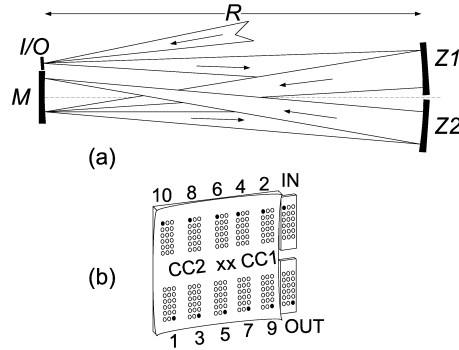


Figure 1. The basic White cell (a) consists of three spherical mirrors. An array of beams is successively re-imaged a fixed number of times on the field mirror (b). The dark spot represents a particular input beam, one of 112.

2. THE QUARTIC TTD WHITE CELL

The White cell described here is a “quartic” White cell [12], meaning that the number of delays N is proportional to the number of bounces m raised to the power of four:

$$N = \left(\frac{m-2}{4} + 1 \right)^4 = \beta^4 \quad (1)$$

The “order” of the cell depends on the number of states that the MEMS has. The MEMS used for this work has three stable states, each mirror being able to tilt to “east,” “west” or flat. A simpler quadratic cell uses two-state MEMS but only provides $N = (m/4)^2 + 3(m/4)$ different delays. If a MEMS has mirrors that can tilt east and west as well as north and south, an octic cell is obtained, providing

$$N = \left(\frac{m-2}{8} + 1 \right)^8 - 1 \quad (2)$$

For example, a quadratic cell with 16 bounces can provide 28 delays, a quartic cell can supply 81 delays in 10 bounces, and an octic cell could do 6561 delays in 18 bounces.* Note that the number of delays is independent of the length of the delays needed.

We implement here a quartic cell. Our MEMS device consists of a single 32×35 array of three-state micromirrors. A mirror tipping “east” sends a beam from one of the null mirrors, say $Z1$, to a new mirror in position $E2$, Figure 2. We replace $E2$ with a dielectric rod, in this case ZnSe, whose thickness provides a delay of $\Delta=312.5$ ps. Its rear surface is reflective, and curved as well as offset to preserve correct imaging of the beam onto the next MEMS mirror. A beam coming from $Z2$ would go to $E1$, which is tilted such that the beam goes to a long mirror train. The beam in this case takes the path $E1, E1a, E1p, E1b, E1q, E1c, E1r$, then returns by the same path to re-image onto the MEMS. The delay

* Actually, the nature of the bounces in an octic cell is that all the east-west switches happen on the first half of the bounces, and the north-south changes happen in the second half, so no individual mirror needs more than three states. Therefore, the same MEMS design used for the quartic cell would also work for the octic cell, if half the mirrors are fabricated with their tilt axes rotated 90°. Thus, the required MEMS chip and drive electronics for an octic cell are no more complicated than those used for the quartic cell.

in this path is 8.4375 ns , or 27Δ , where Δ is the delay increment. Similarly, on the west side there is a silicon rod for a delay of 3Δ (937.5 ps) and a mirror train $W1$, W_a , W_r and back, for a delay of 9Δ (2.1825 ns).

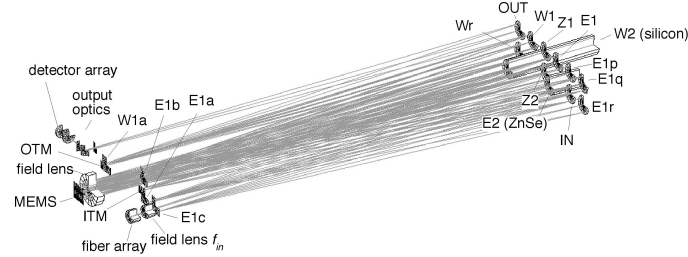


Figure 2. The “quartic” White cell using a three-state MEMS.

In the quartic White cell, each light beam makes 10 round trips, imaging 10 times onto the MEMS. Each beam is allowed to visit any of the delay lines up to two times. Thus, the device provides delays in base 3: for a delay of 0, a beam stays entirely in the null cell ($Z1$, $Z2$, never switches east or west). For a delay of Δ , the beam is sent to $E2$ once, and for a delay of 2Δ it visits $E2$ twice. For 3Δ , the beam goes to $E1$ once and spends the rest of its time in the null cell. With this arrangement, it is possible to get up to 81 delays, for a maximum delay of 25.0000 ns .

The device supports 112 light beams, corresponding to 112 antenna elements in the phased array. The input comes from a custom 7×16 array of single mode fiber, on a $250 \mu\text{m}$ pitch, integrated with a microlens array. The purpose of the microlens array is to magnify the input spots to $60 \mu\text{m}$ radius ($1/e^2$ field), so it has the proper divergence for the subsequent lens train. A field lens corrects the distortion of the edge rays to form a true rectangular array. The input beams then diverge as they go to mirror “IN,” which refocuses the array of beams to spots onto an input turning mirror located on adjacent to $E1a$, instead of adjacent to the MEMS Mirror ($E1A$ is an image of the MEMS). Both the scraper input mirror and $E1a$ are spherical, with the same curvature, but they have different pointing directions. The input beams proceed from the input scraper to $E1$ and thence to the MEMS for the first bounce.

Once “in” the White cell, the beams circulate 10 times, and each time the beams are re-imaged to a 7×16 array of spots on a different area of the MEMS. After 10 bounces, the beams are sent to the west side, where they hit $W1a$, or more accurately an output scraper mirror adjacent to it. The output turning mirror is tipped to direct the beams to “OUT” and from there they are folded by a prism, and sent to the detector array.

3. CONSTRUCTION OF THE WHITE CELL

It will be observed from Figure 2 that there are a large number of optical elements that must be aligned with great precision. With six degrees of positional freedom for each component and their small sizes, integration of the device presents a significant mechanical challenge. In this work, the alignment burden was significantly alleviated by constructing the mirrors in two groups, each from a single substrate. The relative positions of these two blocks was then fixed by a rigid metering structure with a kinematic interface that enables the distance to be repeatable to within 2 micrometers during assembly. Both mirror blocks and the metering structure are made of super-invar substrate for thermal stability and expansion match.

One mirror assembly block, the White Cell, contains twelve objective mirrors (those on the right in Figure 2), including two at the backs of the delay rods, Figure 3(a). Each of these mirrors is 9 mm in diameter, and has either a spherical or toroidal curvature, and each has a slightly different pointing angle that must be accurate to within less than $10 \mu\text{rad}$. With the exception of the delay rods, these were all fabricated on a single substrate using slow-tool diamond turning, described in Section 3.1. Holes for the delay rods were also carved by diamond turning. The substrate was super-Invar with Ni plating. Mirrors $E1a$, $E1b$, $E1c$, $W1a$ (the “front four”), along with the input and output scraper mirrors, are also all spherical and with different pointing angles, and were diamond turned on a second super-Invar substrate. Angles and positions of the delay rods are adjusted separately from the back of the White Cell.

The second mirror assembly block, the Front-4, serves as the anchor platform for all other optical components. It contains the input fiber array, mirrors $E1a$, $E1b$, $E1c$, $W1a$, the MEMS chip, field lens, photodiode receiver interface,

and beam alignment fixtures. The Front-4 plate has a hole for the beams to pass through to the MEMS, and another hole for the input beams. In the figure, an aperture with five small holes is shown, used to align the input fiber array (one hole for each corner and one in the center).

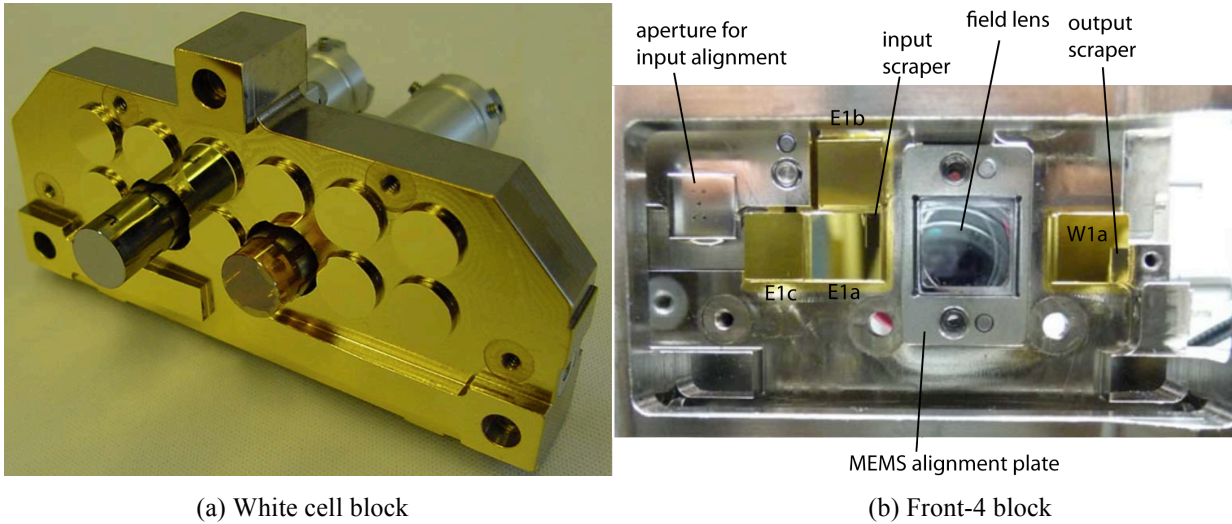


Figure 3. (a) The objective mirrors are all slow-tool diamond turned on a single substrate, with holes to accept the delay rods (b) The remaining mirrors are diamond turned on a second substrate.

3.1 Slow-tool servo diamond turning

The slow-tool servo diamond turning process uses a 350 FG (Freeform Generation) ultra precision machine manufactured by Moore Nanotechnology Inc. It has three linear axes that are equipped with linear laser-scales capable of resolving 8.6 nm at a maximum speed of 1800 mm/min. The straightness on all slides is better than 250 nm. Figure 4a shows the schematic of the slow tool servo diamond turning process that was used to create the objective mirrors.

The mirrors were diamond-turned directly on the nickel-plated substrate, producing a surface finish of 45 nm rms. The surfaces were later coated with Au to enhance reflectivity up to 97% at 1550 nm. The curvatures were measured to be accurate to within 0.1% average error using a Fizeau Interferometer (ADE-PST MiniFIZ 100P-4th) against a reference sphere at 633 nm.

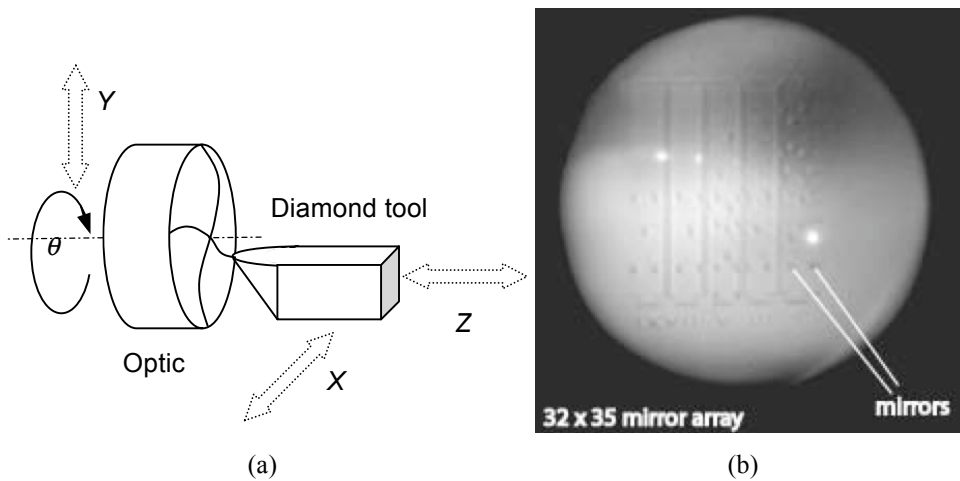


Figure 4. (a) Slow-tool servo diamond turning process. (b) A MEMS substitute for alignment, made by the slow-tool servo diamond turning.

3.2 Alignment

Alignment of the White cell optics is relatively simple due to highly integrated mirror blocks and the precision of the diamond turned alignment features. The first step is to attach the Front-4 and White Cell mirrors to the metering structure using screws. Once the alignment features line up, a mirror block can be removed and replaced without disturbing the alignment of the other block.

The second step is to attach the input fiber array with built in micro-lens and the field lens to the Front-4. This assembly can be adjusted for position and pointing. One alignment plate with five apertures is positioned in front of the input fiber assembly to guide the position alignment. A transparent target plate with grid pattern marking the ideal beam positions is installed at the MEMS field lens location to guide the angular pointing alignment. During alignment, the center and the four corner beams of the 7x16 array are lighted. An IR camera is set up to image the five beams on the grid from the position of the MEMS chip.

Once the input array is aligned and fixed in place, the MEMS chip is installed. The beams now can travel all the way through the White cell, and come out toward the receiver. In place of the receiver is another transparent target plate with a grid pattern. The IR camera is positioned to image this receiver target plate to guide the alignment of the MEMS chip. The MEMS chip can be adjusted for position and clocking only. The focus is fixed due to the collimated nature of the beam pattern after the MEMS field lens. Because each mirror on the MEMS chip can be commanded to tilt to three different angles, it is relatively easy to locate the position of a beam on the MEMS chip surface by toggling individual mirrors and watching for beams on the camera. Knowing the location of the five input beams allows one to optimize the position and clocking of the MEMS chip. The delay rods are aligned in a similar fashion, by directing beams to each rod with the proper MEMS mirror pattern. The final alignment is the receiver, which can be adjusted for position and clocking relative to the Front-4 block. By blinking the four corner beams and monitoring the total photocurrent, the receiver can be oriented correctly to capture all 4 beams and optimized for focus.

3.3 MEMS micromirror array

A MEMS mirror array and supporting drive electronics comprise the switching engine of the delay unit. A photomicrograph of the mirror array and specifications are shown in figure 5. The mirror array was custom-designed for the White Cell application and fabricated in a novel variation of the SUMMIT (Sandia Ultra-planar Multilevel MEMS Technology) with integrated field effect transistors (FETs). The FETs are used to implement a row-column address scheme thus allowing the 2240 electrodes of the array to be addressed with fewer than 120 wires.

The demanding optical specifications of the MEMS mirror array were achieved through careful design and process control. To achieve required mirror flatness (less than 160nm peak-to-valley) the mirror plates are built up from a multi layer stack that provides sufficient stiffness to avoid stress induced mirror curvature. Measured mirror curvatures were less than 50 nm peak-to-valley. To obtain the required mirror tilt angle and angle uniformity across the 8mm x 8.75mm array, mechanical stops are employed in the design. The outer stops are defined simply by the layout geometry but an inner stop is established by a timed dimple etch. This approach very effectively prevents against mirror angle variation due to pattern density effects.

The metalized surface of the mirrors is 240 μm diameter and the mirrors are arrayed on a 250 μm grid to match the spacing of the input fiber array. The metalized mirror surfaces have no etch access holes and a measured peak-to-valley flatness of 50 nm. Each mirror can be switched to one of three positions (east, west or flat) with a nominal tilt angle of 1.4°. Measured mirror tilt angles show angle uniformity across the entire array is better than 0.05°.

Mirror arrays are packaged in a 120-pin ceramic pin grid array (PGA) as shown in Figure 5 (b). Automated die placement ensures that the MEMS array is centered in the package to reduce the optical alignment burden upon delay unit assembly. Automated wire bonding is employed to enable high yield. In the present prototype the MEMS package is not sealed, as even an optimally coated window would severely impact optical loss. Instead the fragile MEMS device is protected in the assembly by the field lens. In a final product the field lens would be used to seal the MEMS package with a suitable ambient for controlled damping of the mirrors irrespective of operating environment.

The MEMS array is driven by an FPGA-based controller that receives mirror position commands via a USB interface from the control PC. The mirror positions are loaded into one of two memory blocks in the FPGA. When the data transfer is completed play out of the row and column signals shifts to the newest data memory. With the dual data

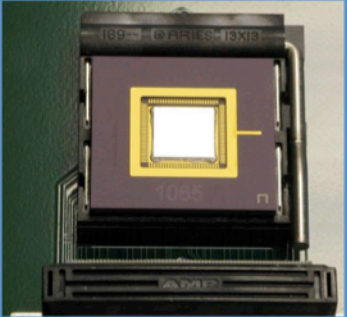
memories the mirror refresh signals are never interrupted by the transfer of new data. Electrode drive signals are played out serially through 16 data lines at a 40MHz aggregate data rate. Four 32-channel serial-to-parallel converters with high voltage outputs (Supertex HV610) shift the logic level signals to the required Row and Column drive levels (typically 20-25V).

On each refresh cycle all electrodes that are “on” are recharged and all electrodes that are “off” are discharged. The discharge of the “off” electrodes ensures that mirrors in the “Flat” position, which has no mechanical stop, are not inadvertently tilted by any stray charge on the electrode. Each electronic refresh cycle takes 45 microseconds. The maximum mirror and array switching speed is established by the release of a mirror from a tilted position. Because this motion is only powered by the stored energy of a torsion flexure, this transition cannot be speeded up by increasing the drive voltage as the transition from flat to tilted can be. Measured switching speeds for mirror arrays to date are 100 μ sec. Prototype mirrors with 60 μ sec switching speeds have been demonstrated.

- **Mirror array layout**
 - 1120 mirrors (32-rows x 35-columns)
 - 240 μ m diameter mirrors, 250 μ m pitch
- **Integrated address electronics**
 - 2240 electrodes (2 per mirror)
 - Packaged in 120 pin PGA
- **Tri-stable mirrors:**
 - $\pm 1.4^\circ$, 0° (flat)
 - Angle deviation $< 0.05^\circ$
- **Mirror flatness:**
 - < 50 nm peak-to valley
- **Functional Mirror Yield: 99-100%**



(a)



(b)

Figure 5. MEMS mirror array specifications, photomicrograph (b) of a fully functional array and photograph of a packaged device in a test socket.

3.4 The detector array

After the programmed delays, the 112 optical beams are reimaged into a 7x16 array onto the photodiode receiver. A microlens array, the same as the one on the input fiber array, focuses each beam onto 9 μ m diameter InGaAs p-i-n diodes (PD), also arranged as a 7x16 array with 250 μ m pitch to match the input beam array. All 112 PDs are connected serially along a traveling wave transmission line that is load-matched at both ends. Because the modulated optical signal carried by each beam contains a pre-set time delay that matches the RF travel delay between PDs, the RF signal traveling in one direction is coherently combined within the 20 GHz receiver bandwidth [13]. This output signal represents the received beam of the antenna array elements.

3.5 The Enclosure

The White Cell block, Front-4 block, and metering structure form a complete, rigid optical assembly, Figure 6, with a natural resonance frequency near 510 Hz. This assembly is mounted to the aluminum enclosure at three points with lock pin screws and vibration isolation pads to reduce mechanical coupling and accommodate for thermal expansion. The

MEMS electronics are in a separate enclosure attached to the top of the box. The entire assembly is approximately 16×5×4 inches in volume.

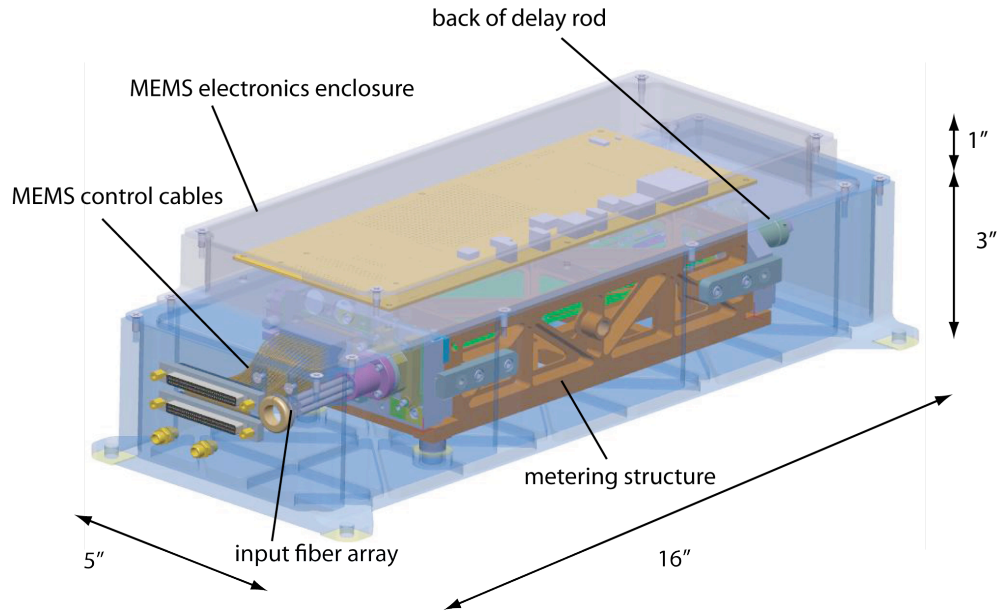


Figure 6. The complete assembly.

4. MEASUREMENTS

4.1 Time delay measurements

The time delays were measured using the apparatus of Figure 7. A 1550 μm laser was modulated with a 1 ns pulse. The beam was then divided, and coupled into two separate fibers in the input array, one via a manually adjustable reference time delay unit. In the White cell, the other beam is delayed by programming the MEMS, and the change in time delay measured. An example measurement is shown in Figure 8. The delay for a beam sent through the null path (all Z1, Z2), experiences a delay relative to the reference of 3.64 ns. The beam, when switched to the silicon delay rod one time, has a delay of 4.58 ns, giving a relative delay of 940 ps (target 937.5 ps). Other results are given in Table 1. The longest three delays are accurate to within experimental error. For the shortest block, the experimental error is 3.2%; the measured value has an error of 4%, still quite close.

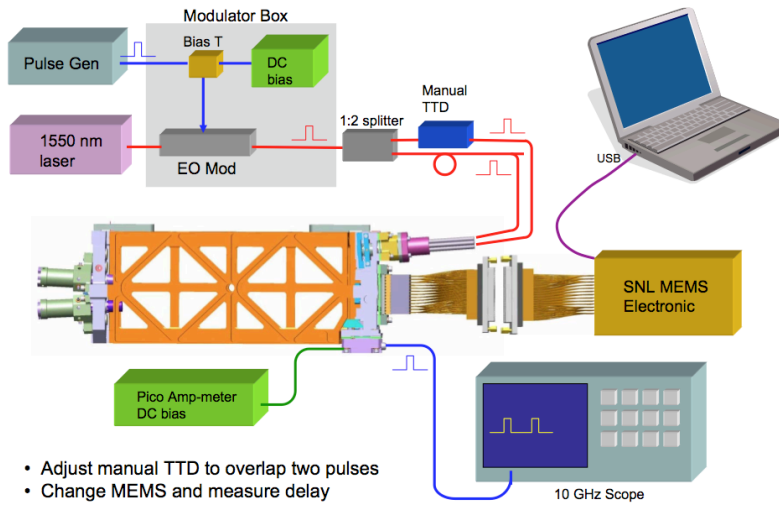


Figure 7. Time delay measurement apparatus.

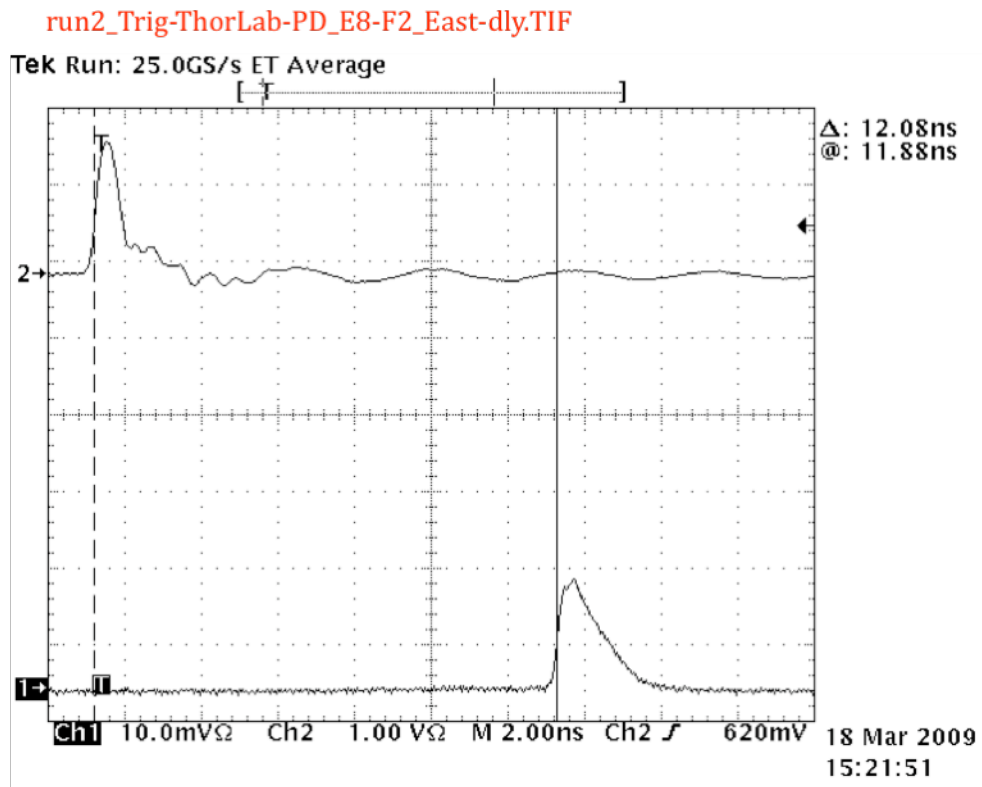


Figure 8. Sample time delay measurement.

Table 1. Time delay measurements.

Path	Measured	Target
ZnSe (Δ)	300 ps \pm 10 ps	312.5 ps
Si (3Δ)	940 ps \pm 10 ps	937.5 ps
W1 (9Δ)	2.80 ns \pm 10 ps	2.8125 ns
E1 (27Δ)	8.44 ns \pm 10 ps	8.4375 ns

4.2 Signal Insertion Loss

Signal insertion loss of the TTD is one of the most important performance parameters that directly affects the system link budget. In our device, this loss consists of the White cell optical insertion loss and the receiver EO conversion loss. The White cell optical insertion loss is the measured optical power difference between the exit of the fiber array and the entrance of the receiver. These locations in our package are accessible to optical power meter, while overlapped beams prevent access to the majority part of the beam path. The receiver EO conversion measures the bias photocurrent produced by a milli-watt of incident light (including transmission through the microlens). Both quantities contain inherent and excess loss. The inherent loss is set by design and material choice, while the excess loss depends on fabrication and alignment quality.

The inherent loss includes the reflectivity of the mirror material, beam diffraction, antireflective coating loss (scattering, absorption), and material absorption (delay rod, lens). These are set by our optical design and material choice. We estimated the inherent loss for a beam in the null delay path to be -5.6dB, dominated by the reflectivity of the MEMS aluminum mirror (R=95.5%, 10 reflections, -2 dB) and the White Cell mirrors (R=96.5%, 13 reflections, -2 dB). The receiver EO conversion was measured with an ideal input beam to be 0.5 mA/mW.

Excess loss includes beam clipping, aberration, and scattering due to misalignment, field curvature, and fabrication defects on mirror surfaces. We observed some beam clipping on the MEMS mirror (240 μ m diameter) and aberration due to operating slightly off-axis through the three field lenses. Beams in the center 75% of the array have relatively small variation (< 3 dB) of loss. For beams along the edges of the 7x16 array, field curvature adds as much as 4 dB of loss. In the receiver, we estimated an excess loss of about -1.2 dB for the null pass beam. This is most likely due to the combined effect of the very short microlens focal length (160 μ m) and the small detector area (9 μ m diameter), resulting in high sensitivity to small tilt error.

The measured average results for five beams shown in Figure 9 are given in Table 2. The average white cell optical insertion loss for the null path was 6.6 dB, or about 1 dB above the estimated inherent loss. However, accumulated wavefront aberrations (mostly focusing error) reduce the EO conversion to 0.37 mW/mA (-1.2 dB loss), resulting in a total insertion loss of 7.82 dB. As the delay path changes, so does the number of mirror reflections and associated losses. The average loss per mirror is between 0.2 dB for the East path, and 0.7 dB for the West path. We do not fully understand the root cause of the difference. It is likely that mirror pointing or surface curvature error is larger in the west path. This difference may also contribute to higher wavefront distortion and the higher receiver excess loss.

The delay dependency of the insertion loss disrupts the beam forming function by varying the contribution from each signal. This dependency can be removed with a programmable optical attenuator in each input fiber. When the delay is changed for a beam, the attenuator is also set to a pre-determined value that compensates for the insertion loss difference. The signal strength from each beam can thus be equalized and maintained independent of the delay.

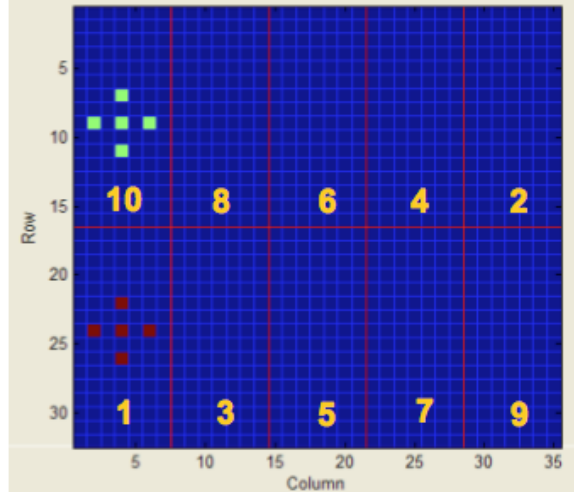


Figure 9. Beams used for the loss measurements. The figure indicates the 10 bounces of the 7×16 input array on the 32×35 mirror array on the MEMS.

Table 2. Loss measurements averaged for five input beams.

Delay path	White Cell Optical Insertion Loss (dB)	Δ dB	Receiver Excess (dB)	Δ dB	Signal Insertion Loss (dB)	# of Mirror reflections	# of Rod reflections
Null (0)	6.6		1.22		7.82	24	
ZnSe (Δ)	6.95	0.35	1.68	0.46	8.63	23	1
Si (3 Δ)	7.58	0.97	1.44	0.22	9.02	23	1
West 1 (9 Δ)	8.62	2.02	1.92	0.70	10.55	28	
East 1 (27 Δ)	8.34	1.74	1.88	0.66	10.22	36	
ZnSe+Si (4 Δ)	7.95	1.35	1.83	0.61	9.78	22	2
West+East(36 Δ)	10.51	3.91	2.43	1.20	12.94	40	

5. CONCLUSION

An optical true-time delay device was demonstrated supporting 81 delays (>6 bits of delay) for 112 antenna elements in a volume of 240 in³. The delays range from 312.5 ps up to 25 ns. Based on the White cell, a free-space system of mirrors for creating long optical paths, the TTD is ultra-compact because the White cell allows many beams to overlap in space. A single MEMS chip, a 32×35 array of three-state tilt mirrors that can tip to $\pm 1/4^\circ$ and 0° provides the switching for all beams, with a switching time of <100 μ sec. The delay paths consist of mirrors trains for long delays and dielectric rods for short delays. Alignment of the many mirrors is greatly simplified by fabricating all the mirrors on two blocks, using slow-tool diamond turning. Surface roughness better than 45 nm rms, mirror curvature accuracy to 0.1%, and pointing accuracy better than 10 μ rad were demonstrated with this process. The optics are held in a super-invar metering structure that has diamond-turned alignment pads that mate to corresponding pads on the mirror blocks. A mirror block can be removed and replaced and all beams will still be completely aligned. The light beams, one for each antenna in the radar array, are input via a 112-element single mode fiber array with integrated microlens. The output is coherently detected using an InGaAs traveling wave detector array beam combiner. Total signal insertion loss from input fiber to detector array was 7.82 dB for the shortest delay path, and 12.94 dB for the path containing the longest lens train. Delays were all within experimental error except the shortest dielectric rod, which was 0.8% outside.

REFERENCES

- [1] Taylor, R., Forrest, S. "Steering of an optically-driven true-time delay phased-array antenna based on a broadband coherent WDM architecture," *IEEE Photonics Technology Letters* 10(1), 144-146 (1998).
- [2] Curtis, D., Sharpe, L., "True time delay using fiber optic delay lines," in *International Symposium Antennas and Propagation 2*, 766-769, (1990).
- [3] Ng, W., Watson, A., "The first demonstration of an optically steered microwave phased array antenna using true-time-delay," *IEEE Journal of Lightwave Technology*, 8(9), 1124-1131 (1991).
- [4] Goutzoulis, A., Davies, K., Zomp, J., Hyrcak, P., and Johnson, A., "Development and field demonstration of a hardware-compressive fiber-optic true-time-delay steering system for phased-array antennas," *Applied Optics* 33(35), 8173-8185 (1994).
- [5] Vidal, B., Madrid, D., Corral, J., Marti, J., "Novel photonic true-time-delay beamformer based on the free spectral range periodicity of arrayed waveguide gratings and fiber dispersion," *IEEE Photonics Technology Letters*, 14(11), 1614-1616 (2002).
- [6] Frankel, F., Esman, R., "Dynamic null steering in an ultrawideband time-steered array antenna," *Applied Optics*, 37(23), 5488-5494 (1998).
- [7] Medberry, J., Matthews, P., "Investigations of linearly chirped fiber Bragg gratings for time-steered array antennas," *Fiber and Integrated optics*, 19, 469-482 (2000).
- [8] Hunter, B., Parker, M., Dexter, J., "Demonstration of a continuously variable true-time delay beamformer using a multichannel chirped fiber grating," *IEEE Transactions on Microwave Theory and Techniques*, 54(1), 861-867 (2006).
- [9] Thai, P., Alphones, A., Lim, R., "A novel simplified dual beam-former using multichannel chirped fiber grating and tunable optical delay lines," *Journal of Lightwave Technology*, 26(15), 2629-2634 (2008).
- [10] Anderson, B.L., Collins, S., Klein, C., Beecher, E., Brown, S., "Optically Produced True-Time Delays for Phased Antenna Arrays," *Applied Optics*, 36,(32), 8493-8503 (1997).
- [11] White, J., "Long optical paths of large aperture," *Journal of the Optical Society of America*, 32(5), 285-288 (1942).
- [12] Anderson, B.L., Mital, R., "Polynomial-based optical true-time delay devices using MEMs," *Applied Optics*, 41(26), 5449-5461 (2002).
- [13] Ho, J., Padilla, J., Gutierrez-Aitken, A., "Wideband coherent combining of photonic RF signals with photodiode array," in *GOMAC Tech. RF Photonics II*, (2004).